Self-supported Bi$_2$MoO$_6$ Nanowall for Photoelectrochemical Water Splitting

Minghong Wu, [†, ‡] *Yuxi Wang,* [†, ‡] *Yang Xu,* [§,‡] *Jie Ming,* [†] *Min Zhou* [§,*] *Rui Xu,* [§] *Qun Fu,* [†] *Yong Lei* [†,§*]

† Institute of Nanochemistry and Nanobiology, School of Environmental and Chemical Engineering, Shanghai University, 200444 P. R. China.

§ Institute of Physics and Macro- and Nanotechnologies MacroNano® (IMN & ZIK), Ilmenau University of Technology, 98693 Ilmenau, Germany. E-mail: yong.lei@tu-ilmenau.de; min.zhou@tu-ilmenau.de

‡ These authors contributed equally to this work.

KEYWORDS: nanowall, alighed nanosheet, bismuth molybdate, PEC water splitting, solar conversion, charge transport efficiency, interfacial charge transfer efficiency

ABSTRACT Nanowall has been regarded as a promising architecture for highly efficient photoelectrochemical (PEC) water splitting due to various superiorities, such as open geometry, highly reactive facets, independent contact with current collector *etc*. Here, vertically aligned Bi_2MoO_6 nanosheet array, which is also called nanowall, is first achieved directly on the ITO glass by a facile solvothermal approach. The structural features not only offer multiple superiorities for PEC processes, and also provide the bridge for in-depth insights of intrinsic features of Bi_2MoO_6 photoanodes. The quantitative analysis of electrochemical process declares that the utilization of photo-generated charges in Bi_2MoO_6 nanowall has been optimized, but the main obstacle comes from the severe bulk recombination and low efficiencies of charge separation. This evaluation both enriches the visual assessment methods, and directs the clear guidance for future improvement, which could serve as a beacon for well-directed and economic photoelectrode amelioration, to shorten the road towards ideal photoelectrodes.

1. INTRODUCTION

Since the first report of the Honda–Fujishima effect in 1972,[1] photoelectrochemical (PEC) water splitting has drawn intensive attention because of the integration of solar energy conversion and collection through one photoelectrode.[2-3] Notwithstanding the considerable research efforts, the insufficient conversion efficiencies limit the progress in practical application. The primary reason comes from the lack of ideal photoelectrodes[4-5] that could harvest enough solar energy, in particular in visible range; separate and collect the photo-generated charges; facilitate the water splitting reaction at the surface, *etc*.. Unfortunately, such a material has never been found yet. How to balance the competing

nature of intrinsic material properties and make full potential of existing candidates remains a major challenge on further optimizing the PEC performance.

Considering that the light absorption is the basic stone for the whole PEC process, it is vital to look for materials with matched band structures with solar spectrum to capture full solar energy, especially from visible light which makes up ~43% of the incoming solar energy. Among various candidates, γ-Bismuth Molybdate (Bi_2MoO_6)[6-7] attract wide attention as a n-type semiconductor response to visible light owing to its narrow band gap of around 2.7 eV and its suitable CB/VB edge positions. γ-Bi_2MoO_6 possesses the Aurivillius structure, where perovskite slabs of corner-sharing $(MoO_6)^{2-}$ octahedrons are sandwiched between $(Bi_2O_2)^{2+}$ layers[8]. Since the first report by Kudo *et al.* to prove the ability of O_2 evolution,[9] much ongoing effort has been completed for solar conversion. Zhu et al. has confirmed that γ-Bi_2MoO_6 exhibits higher photocurrent response than that of other polymorphs due to distortion of Bi–O band.[10] The (010) facets of γ-Bi_2MoO_6 have been further proved as the highly reactive facets in photocatalytic processes.[11] Despite satisfied performance of organic dye degradation[6-8,10-12], the studies of Bi_2MoO_6 for PEC water splitting are relatively limited and the corresponding basic understanding seems insufficient[9,14-17].

To further enhance the PEC performance, considerable efforts have been devoted via various chemical modifications (such as doping,[6,7,11-14,16] heterostructures[8-10,15,17]). Nevertheless, nanoengineering offers us a totally different methodology to improve PEC performance by adjusting the intrinsic electrochemical processes like surface reaction and charge separation/migration. Various morphologies, like mesoporous crystal,[6] hollow spheres,[7] film,[9] plates,[10] belts,[11] *etc.* have been achieved for higher solar conversion

efficiency. Among various architectures, nanowall, which represents vertically aligned nanosheet array,[2, 18-20] stands out because of the following four aspects: (1) The open geometry to allow more contact with electrolyte and elimination of produced O_2; (2) Exposure of highly reactive facets to accelerate the rate of surface reaction because of the structural features and uniform orientation; (3) Independent contact with the current collector to provide a direct pathway for charge transport throughout the electrode; (4) The single-crystalline nature of the nanosheet can depress bulk charge recombination efficiently and provides us the possibilities for quantitative assessment of the intrinsic features of materials. Compared with normal poly-crystalline planar film, nanowall can maximize all the above-mentioned superiorities due to its structural features, which could enrich the understanding of Bi_2MoO_6. Inspired by this concept, an engineered Bi_2MoO_6 nanowall as structurally represented in Scheme 1 is expected as a propitious model to meet the challenging on promoting the performance of Bi_2MoO_6.
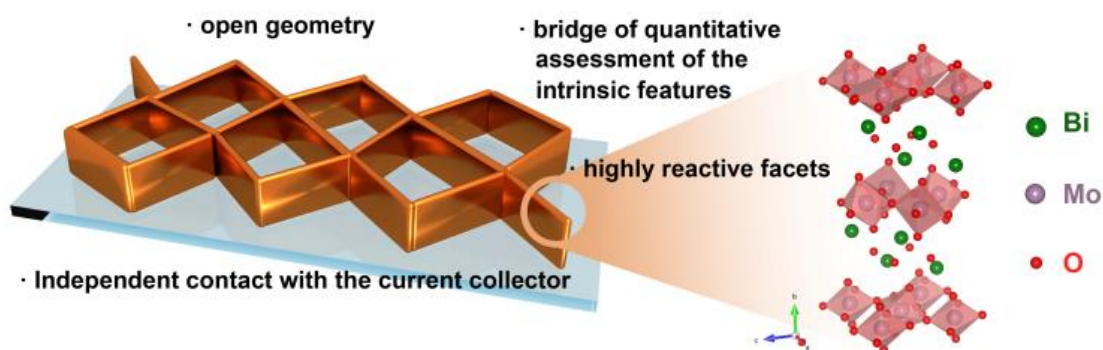
Scheme 1. Schematic representation of the expected superiorities of the integrative nanowall photoelectrodes.[21]

2. EXPERIMENTAL SECTION

4

2.1   Fabrication of Bi_2MoO_6 Films. Bismuth(III) nitrate pentahydrate (Bi $(NO_3)_3 \cdot 5H_2O$) (0.5 mmol) and sodium molybdate dehydrate ($Na_2MoO_4 \cdot 2H_2O$) (0.25 mmol) were respectively dissolved in ethylene glycol (25 ml) with 15 min ultrasonic treatment. After the mixing and stirring for another 1 min, the mixed solution was transferred to a Teflon-lined stainless steel autoclave. A piece of bare tin-doped indium oxide (ITO) glass after cleaning by acetone, ethanol, and distilled water was placed vertically into the autoclave. Then the autoclave was heated to 180 °C for 24 h. After cooling, the glass was took out and washed with distilled water and ethanol, following by drying at 60 °C for 6 h in a vacuum drying oven. The planar film was prepared by drop-coating and annealed at 500 °C for 2 h with the raising rate of 2 °C min^{-1}. The precursor solution consists of Bi $(NO_3)_3 \cdot 5H_2O$ and $(NH_4)_2MoO_4$ in ethylene glycol. For reasonable comparison, the mass loading is the same with that of nanowall.

2.2   Structure and Optical Investigation. The scanning electron microscopy (SEM) images were observed from a JEOL JSM-6700F field emission scanning electron microscope (15 kV). The X-ray diffraction (XRD) patterns were taken by a Philips XQPert Pro Super diffractometer with CuKα radiation (λ=0.154178 nm). The X-ray photoelectron spectroscopy (XPS) data were performed on ESCALAB-MK-II X-ray photoelectron spectrometer with Mg Kα radiation exciting source (1253.6 eV). The high-resolution transmission electron microscopy (HRTEM) measurements were carried out on a JEOL 2010 high-resolution transmission electron microscope performed at 200 kV. UV-vis light absorption spectra were taken on a 950 UV/Vis-NIR Perkin Elmer Lambda spectrophotometer. The EIS measurements were performed on electrochemical station (Shanghai Chenhua Limited, CHI660B).

2.3 Photoelectrochemical Measurement. Photoelectrochemical test systems consist of a three-electrode system with the Bi_2MoO_6 nanowall as photoanode, an Ag/AgCl reference electrode

and a Pt plate as counter electrode. The electrolyte is 0.5 mol L^{-1} Na_2SO_4 solution, which has been introduced with N_2 for 10 min before the measurement to remove the dissolved oxygen. The photoelectrochemical (PEC) performance was recorded on electrochemical station (Shanghai Chenhua Limited, CHI660B) under illumination using a Xe lamp (300 W) with power density of 50 mW cm^{-2} during the measurement (Trusttech Co., Ltd., PLS-SXE300/300UV). The potential range was from -0.2 *vs.* Ag/AgCl to +0.9 V *vs.* Ag/AgCl (scan rate = 10 mV s^{-1}). Incident photon-to-current efficiency (IPCE) measurements were carried out on a QE/IPCE Measurement Kit (Newport, USA). Oriel Tracq Basic V5.0 software was used to control all the kit components automatically. The light source went through a monochromator (74125 Oriel Cornerstone 260 1/4 m). The sampling interval was 10 nm, while the current sampling time was 2 s. A 2931-C dual channel power/current meter and a 71675 calibrated UV silicon photodetector were used to correct the light intensity and record the photocurrent.

2.4 Finite-difference time-domain (FDTD) simulation. We used a commercial FDTD simulation package (FDTD Solutions, Lumerical Solutions Inc.) to simulate the near- field distributions of Bi_2MoO_6 nanowall and planar film. The simulation space was set according to the experimental measurement data. Bi_2MoO_6 nanowall and planar film on ITO glass substrate were modeled and illuminated by a normally incident plane wave source. The Z dimension was truncated by the perfectly matched layers. The mesh size in the simulation region was 1.0 nm. The simulation time and time step were the default parameters of software.

3. RESULTS AND DISCUSSION

To demonstrate the above-mentioned superiorities, herein, a self-supported Bi_2MoO_6 nanowall has been achieved directly on ITO glass through a facile solvothermal approach.

As exhibited in Figure 1a, the whole surface of the ITO glass is covered with free-standing and vertically aligned nanosheets, of which the average thickness is about 10 nm and length is around 350 nm. Close observations on the phase were detected by X-ray Diffraction (XRD) of as-prepared nanowall on ITO glass as shown in Figure 1b. Peaks generated by the ITO substrate are marked with *, being identical with XRD pattern of pure ITO glass (Figure S1). All the other peaks can be assigned to the orthorhombic Bi_2MoO_6, which is consistent with the values of JCPDS card 21-0102. X-ray photoelectron spectra (XPS) further confirms the valence of Bi^{3+} and Mo^{6+}.[22] The details about the preferential growth characteristics of nanowall are proved in Figure 1d by transmission electron microscopy (TEM) image. Obviously, the height and length are consistent with the results of the top-view and cross-section (inset in Figure 1a) SEM analysis. The corresponding fast Fourier transform (FFT) of an individual nanosheet (Figure 1e) implies single crystal nature and can be indexed as [010] zone axis, indicating the similar growth directions and lattice arrangement of each flake. Figure 1f shows the high resolution TEM image of enlarged edge part of the nanosheet in Figure 1d, where the lattice spacing of 0.274 and 0.276 nm between adjacent lattice planes corresponds to the distance of adjacent (100) and (001) crystal planes of Bi_2MoO_6. The acute angle between these two lattices is 90°. All the results further demonstrate that the oriented (010) sheets are vertical to the ITO glass.
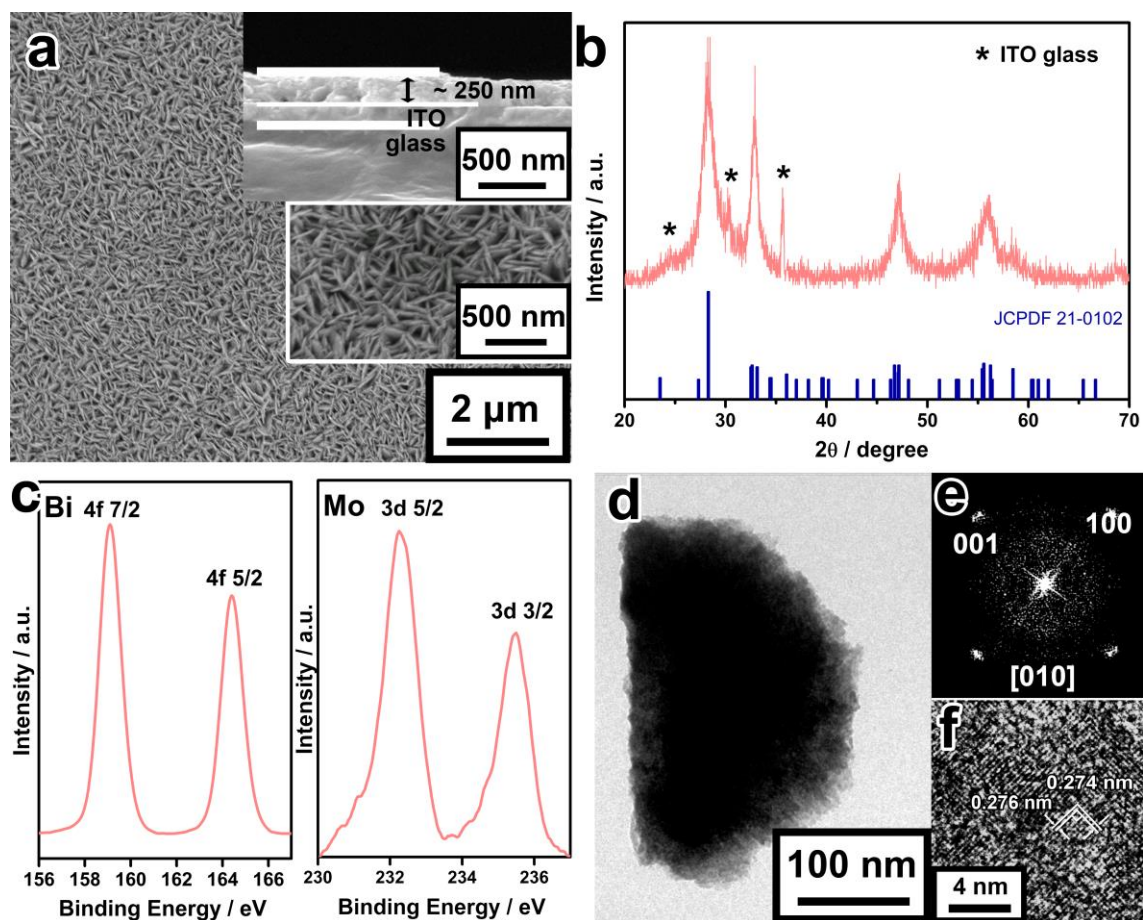
Figure 1. Corresponding characterization of as-prepared nanowall: (a)Typical SEM image; (b) XRD pattern; (c) XPS data; (d) TEM image of nanosheet peeled from the substrate and the corresponding FFT pattern (e). (f) High resolution TEM image of the edge part of nanosheet in (d).

With regard to the growth processes, both the anisotropic crystalline structure and the solvation of ethylene glycol contribute to the as-obtained aligned nanosheet. The possible reactions during the synthesis processes are able be estimated as following:

$$2Bi^{3+} + 2H_2O \rightarrow 2BiO^+ + 4H^+$$

$$2BiO^+ + MoO_4^{2-} \rightarrow Bi_2MoO_6$$
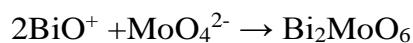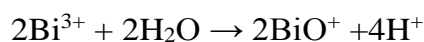
It is well known that the relative chemical potential can determine morphology of nanostructures,[23] and be proportional to the surface-atom ratio. So the final morphology of crystalline material is strongly dependent on the average of dangling bonds per atom over the entire crystal according to the Gibbs-Thompson theory.[24] Determined by its intrinsic crystal structure as shown in Scheme 1 and Figure S2, the orthorhombic Bi_2MoO_6 is built up as alternating $(Bi_2O_2)^{2+}$ layers sandwiched between $(MoO_4)^{2-}$ (corner-shared MoO_6 octahedron) layers, stacking along the b axis. The chains of octahedrons and $Bi_2O_2^{2+}$ equally exist along the [100] and [001] axes, allowing that the (100) and (001) facets perpendicular to these axes have much higher chemical potential than that of other facets, such as (010). Therefore, the growth rate along [100] and [001] is faster, leading to the two-dimensional growth.

Moreover, the products of different reaction time as shown in Figure S3 confirm that the deposition of Bi_2MoO_6 on the ITO substrates is heterogeneous nucleation/growth, while the Bi_2MoO_6 in the bulk reaction solution cannot avoid being generated by homogeneous nucleation. Direct reaction between BiO^+ and MoO_4^{2-} occurred fast and the nuclei grew easily with the solution constantly providing precursors. So the quantity and diffusion rate, at which BiO^+ and MoO_4^{2-} travel to the nucleation sites, have crucial impact on the morphology of final films. And then, as the reaction proceeds, ethylene glycol adheres to the surface of the substrate in form of coordinating bonds with metal ions or hydrogen bonds with O atoms because of the decreased surface energy. Owing to the higher atom densities on (010) facets than other facets, it is inevitable that (010) facets have stronger interaction with ethylene glycol. As expected, if we change ethylene glycol into other solvent like water, only some particles with random packing can be obtained finally as

shown in Figure S4. Overall, following the nucleation and growth with the assistance of ethylene glycol, the anisotropic crystal generates two-dimensional growth, leading to the eventual formation of aligned nanosheet with (010) facet exposed.

To check the potential application for PEC water splitting, the activity of nanowall anode was compared with the reference of planar film, of which the corresponding characterizations are displayed in Figure S5. Although nanowall film was fabricated by a solvothermal method, while the planar film went through high temperature annealing, nanowall possesses comparably good crystallinity in order to easily rule out the crystallinity effect on the performances. As evidenced by normalized plots of peak intensity ratio of different Bi_2MoO_6 facets according to the peak intensity of (222) facet of ITO glass XRD peak intensity in Figure S6, higher XRD peak intensity of nanowall proves that high crystalline materials could be fabricated by solvothermal method.

With regard to the PEC performance shown in Figure 2a, Bi_2MoO_6 nanowall anode yields the satisfied photocurrent densities. Typically, taking the values at the bias of 0.9 V vs. Ag/AgCl for example, the photocurrent density of the nanowall photoelectrode is 75 μA cm^{-2}, which shows 4.7-fold greater than those of planar film and even higher than the performance in previous literatures (Table S1). The superior photocurrent densities can even be observed after continuous illumination for 2700 s (Figure 2b), which originates from the high stability of nanowall skeletons for keeping such a high performance. Remarkably, a profound enhancement of photocurrent densities under low bias is achieved, resulting in a low onset potential. The ratio of photocurrent density between nanowall and planar film can even reach 19 (0.5 V vs. Ag/AgCl). This segment indicates that surface recombination is suppressed with a large extent. The incident photon-to-

electron efficiency (IPCE) mirrors the improvement of the photocurrent densities across the entire wavelength from 300 nm to 500 nm (Figure 2c), especially at visible light range. In order to deeply understand the origin of the superior photocurrent densities, we subtract the influences of light absorption (Figure S7, S8), and use the absorbed photon-to-electron conversion efficiency (APCE) to assess the actual utilization capability of the photons as shown in Figure 2d. APCE can be expressed as the equation: APCE = IPCE / $(1-10^{-A})$, A is the absorptance of film at a specific wavelength. However, the ITO glass has a strong absorption from 300 to 350 nm (Figure S9), which will largely change the true value of A of Bi_2WO_6 in this range. Hence, to accurately assess APCE, we chose 350 nm as the starting point. The large gap between nanowall and planar film evidences that nanowall possesses much higher conversion efficiencies from the photons to photo-generated charges.
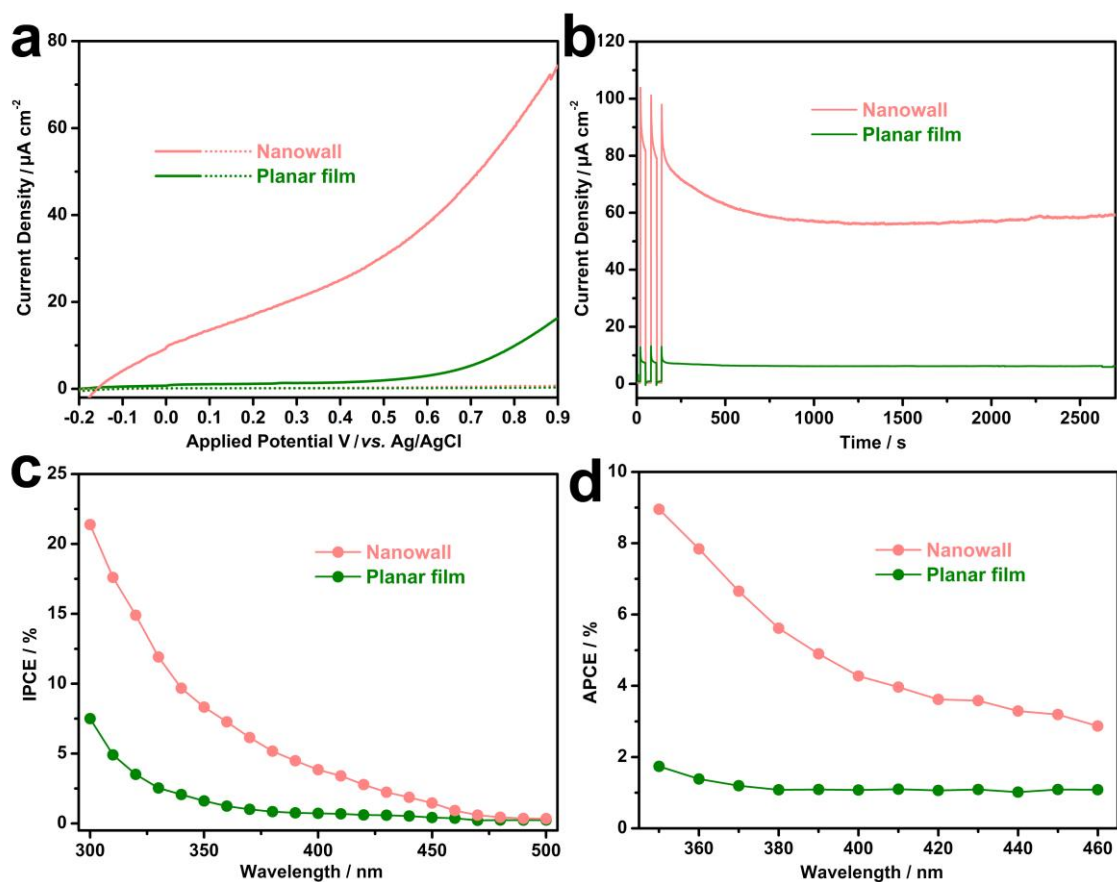
Figure 2. PEC performance of nanowall anode with the reference of planar film. (a) Photocurrent density curves (solid line) and dark-current density curves (dashed line) with different biases at the scan rate = 10 mV s^{-1}. (b) Photocurrent density stability @ 0.8 V *vs.* Ag/AgCl. (c, d) IPCEs and APCEs at 0.6 V *vs.* Ag/AgCl.

Considering that APCE is related to the interfacial charge transfer efficiency ($\eta_{injection}$) and charge transport efficiency ($\eta_{separation}$), to quantitatively reveal the origins, we employ H$_2$O$_2$ as a hole scavenger to rule out the possible influence of surface recombination (*i.e.* $\eta_{injection}$=100%) with no influences on the charge separation process within the space charge layer. Hence, we proceed with this strategy as follows:[20,25]

12

$J_{H2O} = J_{absorbed} \times \eta_{injection} \times \eta_{separation}$

$\eta_{separation} = J_{H2O2} / J_{absorbed}$

$\eta_{injection} = J_{H2O} / J_{H2O2}$

where $J_{absorbed}$ is the photocurrent density resulting from complete conversion of the absorbed photons, $J_{absorbed}$ is 2.1 mA cm^{-2} and 1.9 mA cm^{-2} for nanowall photoelectrode and planar film photoelectrode, respectively, both of which are calculated integrating the absorbance spectrum (Figure S7) with respect to the distributions of power as a function of wavelength in solar spectral irradiance at standard air mass 1.5.[20,25,26] J_{H2O2} is the photocurrent density with the existence of H_2O_2 (Figure S10).

As illustrated in Figure 3a and 3b, nanowall photoanode offers markedly strengthened $\eta_{injection}$ and $\eta_{separation}$ at the entire potentials comparing with those of planar film, hinting at the suppression of surface recombination and bulk recombination. To further prove this enhancement, the interface charge transfer kinetics can be analysed according to electrochemical impedance spectroscopy (EIS). As presented in the Nyquist plots in Figure 3c, nanowall photoanode possesses a dominant semicircle with smaller diameter, the value of which is dependent on charge transfer resistance (R_{ct}) at the interface between Bi_2MoO_6 and electrolyte. With the help of the Randles–Ershler model[20] (inset of Figure 3d), the fitted values of R_{ct} clearly demonstrate much easier interface charge transfer in nanowall photoanode and higher charge utilization.
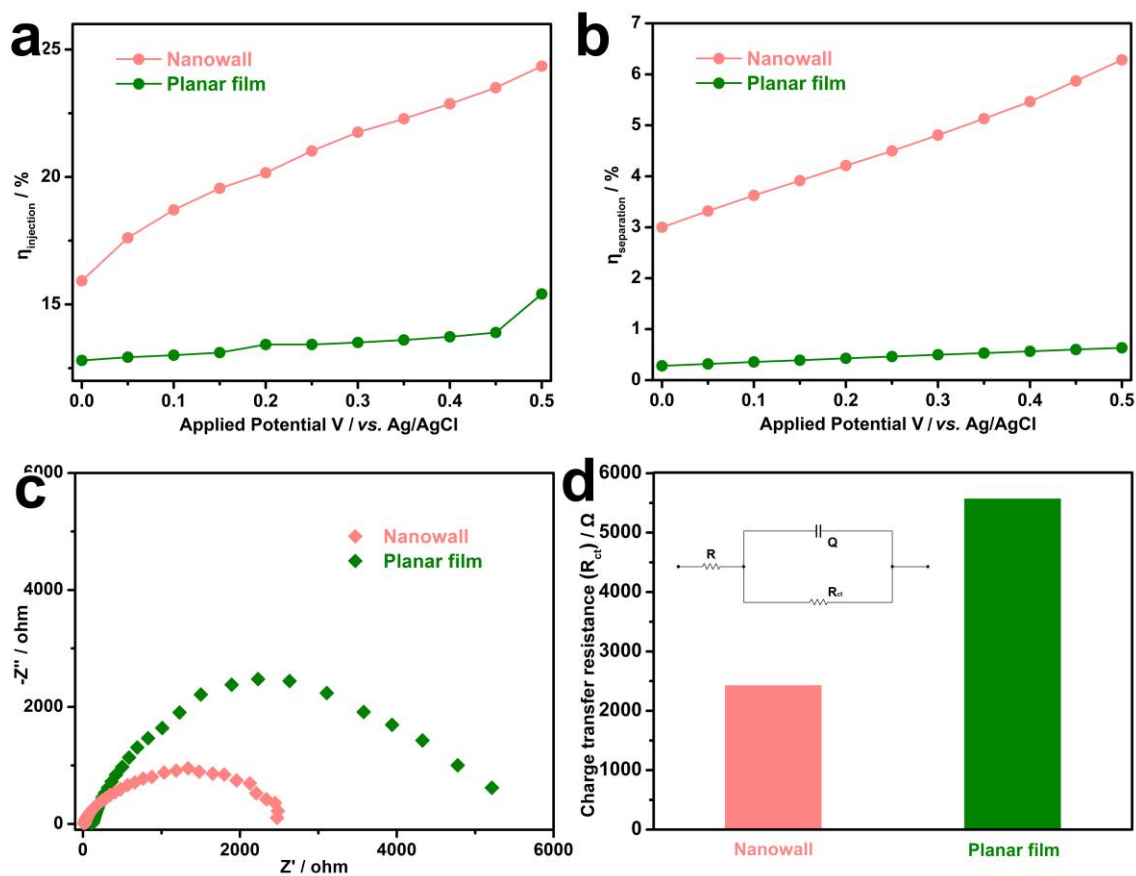
Figure 3. (a) Charge transport efficiency ($\eta_{separation}$). (b) Interfacial charge transfer efficiency ($\eta_{injection}$). (c) EIS Nyquist plots at 0.6 V *vs.* Ag/AgCl. (d) Charge transfer resistance.

Keeping these results in mind, the main aspect that distinguishes the two photoanodes is the different structural features, including the morphology features and the exposure of (010) facets. On one hand, the nano-scaled unit of nanowall leads to the shift of valence band, indicating promising more light harvesting (Figure S11). Moreover, nanowall has open-edge geometry together with a high surface area, which could offer increased light harvesting due to cavity resonance effect (Figure S8), more contact with electrolyte and provide enough room for the elimination of the produced O_2 so that the accumulated

14

holes at the surface can be easily injected to continuously generate O_2, resulting in facile surface reaction. Besides, each nanosheet provides independent contact with the current collector, allowing direct pathway for charge transport throughout the electrode. The fast utilization of holes and transport of electrons make higher efficiencies of charge separation, which could effectively suppress the bulk recombination.

On the other hand, theoretical simulations indicate that the valence band of Bi_2MoO_6 comprise the O 2p orbital. (010) facet possesses the highest density of O atoms[11], which is more favourable to the reacting substrates, like O_2, H_2O or other intermediates. Therefore, the holes at the valence band can be directly utilized by H_2O molecules. The exposure of more active sites lead to efficient separation of charge carriers, and thus the surface reaction can be accelerated. The surface recombination can be eased correspondingly, resulting in improved $\eta_{injection}$ and smaller interface charge transfer resistance. To further prove the activity of (010) facet beyond other facets, we fabricate another nanowall and two nanosheet film with different exposed ratio of (010) facet as reference as shown in Figure S12. To avoid the extra influences from surface features as much as possible, we choose materials with small deviation in morphology parameters to focus on the trend of the influences from facets. The ratio of exposed facet is calculated in an approximate way as described in part 10 and Figure S14 in supporting information according to the distinct morphology features. Corresponding photocurrent density in Figure S13 proves that the PEC performance is increased directly with the exposed ratio of (010) facet, indicating that the reaction activity of (010) facet is much higher than that of other facets. Overall, combining the advantages of morphology features and the exposure of highly reactive

(010) facets, nanowall photoanode exhibits higher $\eta_{separation}$ and $\eta_{injection}$ when comparing with the planar film, giving rise to an improved PEC performance.

For quantitative evaluation the contribution from morphology features and facet, we fabricated Bi_2MoO_6 randomly dispersed nanosheets synthesized in the same chemical environment with similar (010) facet exposure ratio as shown in Figure S12b. The corresponding IPCEs are listed as blue plots in Figure S15a. After normalizing with the values of planar film, we could find the IPCE enhancement factors (Figure S15b) of nanowall (Ew) and nanosheet (Es) photoelectrodes. Considering that the major difference between nanowall and nanosheet film is the structural features, the gap between Ew and Es indicates the contributions of the structural features to the final performance. Meanwhile, the contribution of facet can be roughly estimated by the gap between Es and enhancement factors of planar film (Ep =1). So we could assess the percentage of enhancement from the two kinds of contribution as following:

Percentage of enhancement from nanowall structural features = (Ew-1)/[(Ew-1)+(Es-1)]

Percentage of enhancement from active facet = (Es-1)/[(Ew-1)+(Es-1)]

Shown in Figure S14c is the detailed percentage of the contributions from the structural features (green) and facet (yellow). It is clear that the structural features contribute more to the final enhancement (~70%-75% to ~28%-30% from the influence of facet).

Although these values of photocurrent density show good results to date, the performance is still lower than the classical photoelectrodes such as TiO_2, WO_3, Fe_2O_3 and $BiVO_4$. Taking $BiVO_4$ as a reference, when carefully looking into the data of $\eta_{separation}$ and $\eta_{injection}$, we can find that $\eta_{injection}$ is comparable to those of single crystalline $BiVO_4$ nanowall, but the $\eta_{separation}$ is 10-fold less than that of $BiVO_4$.[20] It can be concluded that the severe bulk

recombination mostly leads to the unsatisfactory PEC performance. Due to the single crystalline nature of Bi_2MoO_6, the bulk recombination mainly results from the intrinsic structure instead of Shockley–Read–Hall recombination process. Future work could be focused on intrinsic structure, such as doping or heterostructures, for further improvement.

4. CONCLUSIONS

In summary, we realize the design of Bi_2MoO_6 nanowall directly on the ITO glass. As return, the PEC performance is comparable among Bi_2MoO_6 photoanodes. The quantitative analysis of electrochemical processes declares that the utilization of photo-generated charges has been optimized, but the main obstacle comes from the severe bulk recombination and low efficiencies of charge separation. Based on this bridge, our understanding is helpful to guide further design and optimization of highly efficient photoelectrodes.

ASSOCIATED CONTENT

Supporting Information. XRD pattern of ITO glass; crystalline structure of Bi_2MoO_6; products with different reaction time; products with the existence of water; characterization of planar film; comparison of PEC performance of Bi_2MoO_6 photoelectrodes; light absorption spectra; photocurrent density in the presence of H_2O_2; PEC performance related to different exposed ratio of (010) facet; quantitative evaluation of the contribution from morphology features and facet. This material is available free of charge via the Internet at http://pubs.acs.org.

AUTHOR INFORMATION

Corresponding Author

*E-mail: yong.lei@tu-ilmenau.de; min.zhou@tu-ilmenau.de

Author Contributions

‡ M. Wu, Y. X. W and Y. Xu contributed equally to this work.

Notes

The authors declare no competing financial interest.

REFERENCES

(1)   Fujishima, A.; Honda, K., Electrochemical Photolysis of Water at a Semiconductor Electrode. *Nature* **1972**, *238*, 37-38.

(2)   Zhou, M.; Lou, X. W.; Xie, Y., Two-dimensional Nanosheets for Photoelectrochemical Water Splitting: Possibilities and Opportunities. *Nano Today* **2013**, *8*, 598-618.

(3)   Walter, M. G.; Warren, E. L.; McKone, J. R.; Boettcher, S. W.; Mi, Q.; Santori, E. A.; Lewis, N. S., Solar Water Splitting Cells. *Chem. Rev.* **2010**, *110*, 6446-6473.

(4)   Osterloh, F. E., Inorganic Nanostructures for Photoelectrochemical and Photocatalytic Water Splitting. *Chem. Soc. Rev.* **2013**, *42*, 2294-2320.

(5)   Liu, R.; Lin, Y.; Chou, L.-Y.; Sheehan, S. W.; He, W.; Zhang, F.; Hou, H. J. M.; Wang, D., Water Splitting by Tungsten Oxide Prepared by Atomic Layer Deposition and Decorated with an Oxygen-Evolving Catalyst. *Angew. Chem.* **2011**, *123*, 519-522.

(6)   Hao, Y.; Dong, X.; Zhai, S.; Wang, X.; Ma, H.; Zhang, X., Towards Understanding the Photocatalytic Activity Enhancement of Ordered Mesoporous Bi_2MoO_6 Crystals Prepared via a Novel Vacuum-assisted Nanocasting Method. *RSC Adv.* **2016**, *6*, 35709-35718.

(7)   Tian, G.; Chen, Y.; Zhou, W.; Pan, K.; Dong, Y.; Tian, C.; Fu, H., Facile Solvothermal Synthesis of Hierarchical Flower-like Bi_2MoO_6 Hollow Spheres as High Performance Visible-Light Driven Photocatalysts. *J. Mater. Chem.* **2011**, *21*, 887-892.

(8)   Lou, S. N.; Scott, J.; Iwase, A.; Amal, R.; Ng, Y. H., Photoelectrochemical Water Oxidation using a Bi_2MoO_6/MoO_3 Heterojunction Photoanode Synthesised by Hydrothermal Treatment of an Anodised MoO_3 Thin Film. *J. Mater. Chem. A* **2016**, *4*, 6964-6971.

(9)   Shimodaira, Y.; Kato, H.; Kobayashi, H.; Kudo, A., Photophysical Properties and Photocatalytic Activities of Bismuth Molybdates under Visible Light Irradiation. *J. Phys. Chem. B* **2006**, *110 (36)*, 17790-17797.

(10)   Zhang, L.; Xu, T.; Zhao, X.; Zhu, Y., Controllable Synthesis of Bi_2MoO_6 and Effect of Morphology and Variation in Local Structure on Photocatalytic Activities. *Appl. Catal. B: Environ.* **2010**, *98 (3–4)*, 138-146.

(11)   Long, J.; Wang, S.; Chang, H.; Zhao, B.; Liu, B.; Zhou, Y.; Wei, W.; Wang, X.; Huang, L.; Huang, W., Bi_2MoO_6 Nanobelts for Crystal Facet-Enhanced Photocatalysis. *Small* **2014**, *10*, 2791-2795.

(12)   Dai, Z.; Qin, F.; Zhao, H.; Ding, J.; Liu, Y.; Chen, R., Crystal Defect Engineering of Aurivillius Bi_2MoO_6 by Ce Doping for Increased Reactive Species Production in Photocatalysis. *ACS Cata.* **2016**, 6, 3180-3192.

(13)   Zhou, L.; Yu, M.; Yang, J.; Wang, Y.; Yu, C., Nanosheet-Based $Bi_2Mo_xW_{1-x}O_6$ Solid Solutions with Adjustable Band Gaps and Enhanced Visible-Light-Driven Photocatalytic Activities. *J. Phys. Chem. C* **2010**, *114*, 18812-18818.

(14)   Zhang, X.-B.; Zhang, L.; Hu, J.-S.; Huang, X.-H., Facile Hydrothermal Synthesis and Improved Photocatalytic Activities of Zn^{2+} doped Bi_2MoO_6 Nanosheets. *RSC Adv.* **2016**, *6*, 32349-32357.

(15)   Ma, Y.; Jia, Y.; Wang, L.; Yang, M.; Bi, Y.; Qi, Y., $Bi_2MoO_6/BiVO_4$ Heterojunction Electrode with Enhanced Photoelectrochemical Properties. *Phys. Chem. Chem. Phys.* **2016**, *18*, 5091-5094.

(16)   Di, J.; Xia, J.; Ji, M.; Li, H.; Xu, H.; Li, H.; Chen, R., The Synergistic role of Carbon Quantum Dots for the Improved Photocatalytic Performance of Bi_2MoO_6. *Nanoscale* **2015**, *7*, 11433-11443.

(17)   Jin, B.; Jiao, Z.; Bi, Y., Efficient Charge Separation between Bi_2MoO_6 Nanosheets and ZnO Nanowires for Enhanced Photoelectrochemical Properties. *J. Mater. Chem. A* **2015**, 3, 19702-19705.

(18)   Zhou, M.; Bao, J.; Tao, M.; Zhu, R.; Zeng, Y.; Wei, Z.; Xie, Y., Rational Design of the Nanowall Photoelectrode for Efficient Solar Water Splitting. *Chem. Comm.* **2012**, *48*, 3362-3364.

(19)   Zhou, M.; Zhang, S.; Sun, Y.; Wu, C.; Wang, M.; Xie, Y., C-oriented and {010} Facets Exposed $BiVO_4$ Nanowall Films: Template-Free Fabrication and their Enhanced Photoelectrochemical Properties. *Chem. Asian J.* **2010**, *5*, 2515-2523.

(20)   Zhou, M.; Bao, J.; Bi, W.; Zeng, Y.; Zhu, R.; Tao, M.; Xie, Y., Efficient Water Splitting via a Heteroepitaxial $BiVO_4$ Photoelectrode Decorated with Co-Pi Catalysts. *ChemSusChem* **2012**, *5*, 1420-1425.

(21)   Momma, K.; Izumi, F., VESTA 3 for Three-dimensional Visualization of Crystal, Volumetric and Morphology Data. *J. Appl. Crystal.* **2011**, *44*, 1272-1276.

(22)   Hao, Z.; Xu, L.; Wei, B.; Fan, L.; Liu, Y.; Zhang, M.; Gao, H., Nanosize α-Bi_2O_3 Decorated Bi_2MoO_6 via an Alkali Etching Process for Enhanced Photocatalytic Performance. *RSC Adv.* **2015**, *5*, 12346-12353.

(23)   Peng, Z. A.; Peng, X., Nearly Monodisperse and Shape-Controlled CdSe Nanocrystals via Alternative Routes: Nucleation and Growth. *J. Am. Chem. Soc.* **2002**, *124*, 3343-3353.

(24)   Yu, S. H.; Liu, B.; Mo, M. S.; Huang, J. H.; Liu, X. M.; Qian, Y. T., General Synthesis of Single-Crystal Tungstate Nanorods/Nanowires: A Facile, Low-Temperature Solution Approach. *Adv. Funct. Mater.* **2003**, *13*, 639-647.

(25)   Dotan, H.; Sivula, K.; Gratzel, M.; Rothschild, A.; Warren, S. C., Probing the Photoelectrochemical Properties of Hematite (α-Fe_2O_3) Electrodes using Hydrogen Peroxide as a Hole Scavenger. *Energy Environ. Sci.* **2011**, *4*, 958-964.

(26)   Tilley, S.; David., Cornuz, M.; Sivula, K. ; Grätzel, M. Light-Induced Water Splitting with Hematite: Improved Nanostructure and Iridium Oxide Catalysis. *Angew. Chem.*, **2010**, *122*: 6549–6552